Design and Analysis of a Multilayer Meander Line Circular Polarization Selective Structure

Ericsson, Andreas; Sjöberg, Daniel

2017

Document Version:
Manuskriptversion före sakkunniggranskning

CODEN:LUTEDX/(TEAT-7250)/1-26/(2017)

Design and Analysis of a Multilayer Meander Line Circular Polarization Selective Structure

Andreas Ericsson and Daniel Sjöberg

Electromagnetic Theory
Department of Electrical and Information Technology
Lund University
Sweden

(TEAT-7250)/1-26/(2017): A.Ericsson, D. Sjöberg, A Multilayer Meander Line Circular Polarization Selective Structure

Andreas Ericsson
andreas.ericsson@eit.lth.se

Department of Electrical and Information Technology
Electromagnetic Theory
Lund University
P.O. Box 118
SE-221 00 Lund
Sweden

Daniel Sjöberg
daniel.sjoberg@eit.lth.se

Department of Electrical and Information Technology
Electromagnetic Theory
Lund University
P.O. Box 118
SE-221 00 Lund
Sweden

This is an author produced preprint version of the paper:

A. Ericsson and D. Sjöberg. "Design and analysis of a multilayer meander line circular polarization selective structure". *IEEE Trans. Antennas Propag.* 65 (8) (2017): pp. 4089–4101

from http://dx.doi.org/10.1109/tap.2017.2710207

This paper has been peer-reviewed but does not include the final publisher proof-corrections or journal pagination.
Homepage `http://www.eit.lth.se/teat`

Editor: Mats Gustafsson

Abstract

We present a non-resonant circular polarization selective structure based on multiple layers of stacked meander line sheets arranged closely after each other. The structure has a total thickness of 13.5 mm (0.68 wavelengths at center frequency 15 GHz) and is realized by cascading printed circuit boards interspaced with a low permittivity foam material, and the different layers are bonded together with thin layers of adhesive spray. A design procedure is presented that can be used to optimize the proposed structure based on its target band of operation. Based on this method, an optimized design has been simulated and the structure shows a return loss and insertion loss better than 0.5 dB, and axial ratio in transmission and reflection better than 0.78 dB, over a fractional bandwidth of 45.8 % at normal incidence, fully covering the K_u-band 12–18 GHz. The functionality of the structure has been verified experimentally through measurements, both in reflection and transmission, with a total bandwidth of 42.0 %, covering 86.7 % of the K_u-band. The simulated performance at oblique angles of incidence shows significant improvements when compared to classical resonant circular polarization selective structures.

1 Introduction

The constant demand for increased data rates in satellite communication systems is a strong driving force in the development of new technology [16, 25]. Meanwhile, the physical aperture of a satellite available for the communication payload, such as communication antennas, receivers and transmitters, is very limited. This implies that a crucial task to achieve maximum performance of a communication satellite is to optimize the use of the available aperture. In recent years, different schemes have been identified to increase the data throughput of a satellite communication system, and it has been shown that the total throughput can be significantly improved by utilizing polarization- and frequency reuse schemes [4, 5, 16, 25, 28].

Polarization reuse can be achieved in linear polarization simply by separating signals using a strip grid of conducting wires, where signals polarized parallel to the wires are reflected and signals polarized perpendicular to the wires are transmitted [5]. In satellite communication systems, it is preferable to utilize circularly polarized signals, which eliminates the problem of aligning receiving antennas with the polarization of the incident signals. This implies that it is crucial to be able to filter signals of different circular polarization (CP). Unfortunately, this is not as easy as filtering signals of linear polarization. It was proven in [27] that in order for a structure to possess circular polarization selectivity, it has to have an extent in the direction of propagation of the incident signal. In this paper, the focus is set on structures that possess circular polarization selectivity both in transmission and reflection.

Many circular polarization selective structures (CPSS) have been presented over the last 50 years. The first design was presented by Pierrot in 1966, and is based on a periodic array of one wavelength long resonant wires bent in the shape of a

crank, and it has a bandwidth of about 10% at normal incidence [24]. This type of structure has been realized in different shapes, using innovative manufacturing techniques, and measured in transmission in [12, 20, 21] and both in transmission and reflection in [28]. Recently, a similar structure was presented in [26], where the concept behind the Pierrot element is utilized to create a reciprocal CPSS molecule. In 1991, Tilston presented a resonant structure based on two one half wavelength long wires connected with a transmission line with physical length of a quarter wavelength and electrical length of half a wavelength [35]. The bandwidth of this structure is comparable to the Pierrot design, but it shows a slightly improved stability with respect to variations in the angle of incidence. Another resonant design, based on continuous wires bent in the shape of helices, was presented by Morin in 1996 [23].

A common remark on these structures, which we refer to as classical resonant CPSS designs, is that they all have a relatively narrow bandwidth and their performance deteriorate at oblique angles of incidence. In [27], these designs were evaluated and it was concluded that structures that possess a two-fold rotational symmetry possess an improved stability with respect to the angle of incidence. This idea was utilized in [10], where a modified version of the Morin CPSS in [23] consisting of closely spaced helices was presented. The bandwidth of this design is comparable to previous resonant CPSS, about 10%, but a significant improvement in angular stability is achieved.

As opposed to the classical resonant designs, a non-resonant CPSS concept realized by cascading two polarizers and one linear polarization diplexer is presented by Joyal and Laurin in [17, 18, 19]. Each polarizer consists of three layers of printed meander lines, leading to a total of seven layers including the wire grid diplexer. The improvement in bandwidth of this structure is significant compared to the classical designs. The total thickness of this structure is 24 mm, which corresponds to 1.5 wavelengths ($1.5\lambda_0$) at the center frequency of 19 GHz, and it shows a 3 dB axial ratio fractional bandwidth of 26%. However, for every layer that is introduced the insertion loss of the CPSS increases, and the fact that the structure is relatively thick with respect to the wavelength of the incident signal is undesirable. An alternative design utilizing the same concept (polarizer, grid diplexer, polarizer) was recently presented in [2, 3], where a wider bandwidth and an improved angle of incidence stability are achieved compared to [17, 18, 19]. However, this requires a more complex structure composed of ten substrates and fourteen printed layers, which negatively affects the overall insertion loss. Also, the axial ratio of this design is on the order of 4-5 dB, which does not meet the strict requirements of satellite communication systems.

In the last ten years, novel resonant CPSS designs without conducting vias have been presented. In [34] a three layer CPSS utilizing coupling through L-shaped traces is demonstrated, and in [33] a structure consisting of two closely spaced layers of split ring resonators is introduced. Recently, a multilayer CPSS consisting of tensor impedance surfaces was presented in [30]. All these designs provide a very narrow bandwidth, but the structures can be made very thin with respect to the center wavelength of operation.

Structures possessing circular polarization selectivity have also been developed for optical frequencies. A design for visible light based on rotating dipoles is presented in [37], where it is shown that the performance of the structure improves with the number of layers, but only transmission results are given. In [13], another design for optical frequencies is presented, consisting of metal helices attached to a substrate. This structure has a wide bandwidth but the helices become very large when scaled to microwave frequencies, where each spiral has an electrical length corresponding to multiple wavelengths of the incident signal. Also, the performance of this structure was only investigated in transmission.

It can be concluded that all the circular polarization selective designs satisfying strict demands presented up to date have a relatively narrow frequency band of operation, and are sensitive to variations in the angle of incidence, especially the resonant structures based on bent wire cranks [27]. In [9], it was shown that, at oblique angles of incidence, the performance of a CPSS is also strongly dependent on what incidence plane is considered, and that the classical designs like those by Pierrot, Tilston, and Morin all have a preferred incidence plane of operation. This implies that to meet the high requirements for satellite communication applications, a novel CPSS should have a wide bandwidth and show significant stability with respect to variations in the angle of incidence. Also, a CPSS with multiple incidence planes of operation would improve the design freedom of the feed placement when implementing the structure in a satellite communication system.

In this paper, we present a thorough analysis of a novel non-resonant CPSS that was first presented in [32]. This design possesses a significantly improved bandwidth compared to previous designs and it shows promising stability with respect to variations in the angle of incidence. Simulation data indicate that, due to the high degree of symmetry of the structure, the design has multiple incidence planes of operation. This is a useful feature when implementing a CPSS in a satellite communication system. Our novel design is based on a material concept first presented in [36] for a polarization rotator, and is similar to the structure in [17, 18, 19], with an electrical design based on rotating meander lines enabling the use of fewer layers, resulting in a thinner multilayer structure than [18]. The bandwidth of our design is presented in Table 1, where a performance comparison to some of the CPSS presented up to date is presented, based on the design requirements from [4, 29]. Since not all designs were made with these strict requirements in mind, we also present results for relaxed requirements to give a fair comparison. The bandwidth of most competing designs is mainly limited by high insertion loss, especially with respect to the strict design requirements in Table 1.

The paper is organized as follows: in Section II, the theory of designing CPSS from linear elements is presented. By calculating the scattering matrix components of cascaded linear grids with a relative rotation, and transforming the scattering matrix to a circular polarization representation, the functionality of the structure is derived. In Section III, our novel design is presented and its possible applications in satellite communication systems are discussed. The optimization scheme that was used to generate the end design is described in Section IV, and simulation results of the optimized design are presented in Section V. Measurement verification of

Table 1: Bandwidth over which each CPSS satisfies all requirements: IL and RL better than 0.5 dB, and AR_t and AR_r better than 0.78 dB, or the relaxed requirements of IL and RL better than 1.0 dB and AR_t and AR_r better than 3.0 dB.

Reference	Simulated/ measured	Bandwidth strict (%)	Bandwidth relaxed (%)	Thickness
Fusco [12]	measured	0.0	2.0	$0.25\lambda_0$
Lopez [20]	measured	0.0	< 5.0	$0.25\lambda_0$
Sanz-Fernandez [28]	measured	7.0	11.0	$0.25\lambda_0$
Ericsson[10]	simulated	8.0	20.0	$0.25\lambda_0$
Joyal [18]	measured	3.0	26.0	$1.50\lambda_0$
Abadi [2]	simulated	0.0	<20.0	$0.23\lambda_0$
Tarn [34]	measured	0.0	<5.0	$0.18\lambda_0$
Present work	simulated	45.9	56.1	$0.68\lambda_0$
	measured	42.0	53.7	

the functionality of the structure is presented in Section VI, and some concluding remarks are given in Section VII.

2 Circular Polarization Selectivity From Linear Elements

The archetypical linearly polarized element is a strip. The reflection coefficient of a periodic arrangement of strips, illuminated perpendicularly to the surface, is dependent on the polarization of the incident field. This type of scattering problem can be modeled using transmission line theory, where the strip grid is modeled as a lumped capacitance or inductance utilizing approximate expressions in [22, p.227]

$$L \approx \frac{\mu_0 a}{2\pi} \ln\left(\frac{2a}{\pi w}\right) \qquad C \approx 4\frac{\epsilon_0 a}{2\pi} \ln\left(\frac{2a}{\pi d}\right) \tag{2.1}$$

where a is the period of the strips, w is the strip width, and d is the gap between the strips, as can be seen in Fig. 1. The permeability and permittivity of vacuum are denoted by μ_0 and ϵ_0, respectively. These expressions are valid when $a \ll \lambda$, and more or less complicated correction terms can be found in [22], but the range of possible L and C is characterized rather well by these simple formulas. In general, the reflection coefficient for a transmission line with characteristic admittance Y_0 which is shunted with an admittance Y is

$$r = \frac{Y_0 - (Y + Y_0)}{Y_0 + Y + Y_0} = \frac{-Y/(2Y_0)}{1 + Y/(2Y_0)} \tag{2.2}$$

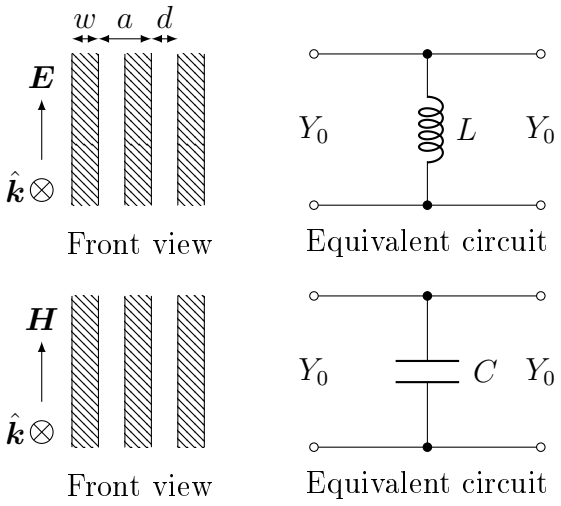

Figure 1: Equivalent circuit models for scattering against infinitely thin metal strips [31], where the direction of propagation is given by $\hat{\boldsymbol{k}}$. In the scenario at the top, where the incident electric field is polarized parallel to the strips, the structure is perceived as a shunt inductance and in the case at the bottom, where the magnetic field is polarized parallel to the strips, the structure is perceived as a shunt capacitance.

where $Y = 1/(\mathrm{j}\omega L)$ for an inductive strip and $Y = \mathrm{j}\omega C$ for a capacitive strip. For a plane wave impinging on the strip grid at normal incidence, we have $Y_0 = \sqrt{\epsilon_0/\mu_0} = 2.65\,\mathrm{mS}$.

Assume a linearly polarized element, with zero thickness in the z-direction, with reflection coefficients r_x and r_y in its principal polarizations x and y modeled by an inductance L and a capacitance C

$$r_x = \frac{Y_0 - (Y_0 + 1/(\mathrm{j}\omega L))}{Y_0 + Y_0 + 1/(\mathrm{j}\omega L)} = -\frac{1}{1 + \mathrm{j}\omega L 2Y_0} \tag{2.3}$$

$$r_y = \frac{Y_0 - (Y_0 + \mathrm{j}\omega C)}{Y_0 + Y_0 + \mathrm{j}\omega C} = -\frac{\mathrm{j}\omega C/(2Y_0)}{1 + \mathrm{j}\omega C/(2Y_0)} \tag{2.4}$$

Given zero thickness, the transmission coefficients are then $t_{x,y} = 1 + r_{x,y}$. When tilting the element at an angle φ from the x-axis, the scattering matrix in linear

polarization is given by

$$S_{\text{grid}}^{\text{LP}} = \begin{pmatrix} S_{11}^{\text{XX}} & S_{11}^{\text{XY}} & S_{12}^{\text{XX}} & S_{12}^{\text{XY}} \\ S_{11}^{\text{YX}} & S_{11}^{\text{YY}} & S_{12}^{\text{YX}} & S_{12}^{\text{YY}} \\ S_{21}^{\text{XX}} & S_{21}^{\text{XY}} & S_{22}^{\text{XX}} & S_{22}^{\text{XY}} \\ S_{21}^{\text{YX}} & S_{21}^{\text{YY}} & S_{22}^{\text{YX}} & S_{22}^{\text{YY}} \end{pmatrix} = \begin{pmatrix} \cos\varphi & -\sin\varphi & 0 & 0 \\ \sin\varphi & \cos\varphi & 0 & 0 \\ 0 & 0 & \cos\varphi & -\sin\varphi \\ 0 & 0 & \sin\varphi & \cos\varphi \end{pmatrix} \begin{pmatrix} r_x & 0 & t_x & 0 \\ 0 & r_y & 0 & t_y \\ t_x & 0 & r_x & 0 \\ 0 & t_y & 0 & r_y \end{pmatrix} \begin{pmatrix} \cos\varphi & \sin\varphi & 0 & 0 \\ -\sin\varphi & \cos\varphi & 0 & 0 \\ 0 & 0 & \cos\varphi & \sin\varphi \\ 0 & 0 & -\sin\varphi & \cos\varphi \end{pmatrix} \tag{2.5}$$

where each entry in the matrix is defined as $S_{mn}^{kl} = E_m^k / E_{n0}^l$, E_m^k is the total outgoing field at port m with the polarization k and E_{n0}^l is the incident field from port n with the polarization l, and when all other ports are not excited and terminated with their characteristic impedance. The scattering matrix in circular polarization, using the IEEE standard [15, p.61-77], $\mathrm{e}^{\mathrm{j}\omega t}$ time convention, and defining the z-axis as pointing from port 1 towards port 2, can be identified as

$$S^{\text{CP}} = \begin{pmatrix} S_{11}^{\text{RR}} & S_{11}^{\text{RL}} & S_{12}^{\text{RR}} & S_{12}^{\text{RL}} \\ S_{11}^{\text{LR}} & S_{11}^{\text{LL}} & S_{12}^{\text{LR}} & S_{12}^{\text{LL}} \\ S_{21}^{\text{RR}} & S_{21}^{\text{RL}} & S_{22}^{\text{RR}} & S_{22}^{\text{RL}} \\ S_{21}^{\text{LR}} & S_{21}^{\text{LL}} & S_{22}^{\text{LR}} & S_{22}^{\text{LL}} \end{pmatrix} = \frac{1}{2} \begin{pmatrix} 1 & -\mathrm{j} & 0 & 0 \\ 1 & \mathrm{j} & 0 & 0 \\ 0 & 0 & 1 & \mathrm{j} \\ 0 & 0 & 1 & -\mathrm{j} \end{pmatrix} \begin{pmatrix} S_{11}^{\text{XX}} & S_{11}^{\text{XY}} & S_{12}^{\text{XX}} & S_{12}^{\text{XY}} \\ S_{11}^{\text{YX}} & S_{11}^{\text{YY}} & S_{12}^{\text{YX}} & S_{12}^{\text{YY}} \\ S_{21}^{\text{XX}} & S_{21}^{\text{XY}} & S_{22}^{\text{XX}} & S_{22}^{\text{XY}} \\ S_{21}^{\text{YX}} & S_{21}^{\text{YY}} & S_{22}^{\text{YX}} & S_{22}^{\text{YY}} \end{pmatrix} \begin{pmatrix} 1 & 1 & 0 & 0 \\ -\mathrm{j} & \mathrm{j} & 0 & 0 \\ 0 & 0 & 1 & 1 \\ 0 & 0 & \mathrm{j} & -\mathrm{j} \end{pmatrix} \tag{2.6}$$

By combining the expressions (2.5)-(2.6) and collecting the results, we get the following representation of the scattering matrix in circular polarization

$$S_{\text{grid}}^{\text{CP}} = \frac{r_x - r_y}{2} \begin{pmatrix} \mathrm{e}^{-2\mathrm{j}\varphi} & 0 & 0 & \mathrm{e}^{-2\mathrm{j}\varphi} \\ 0 & \mathrm{e}^{2\mathrm{j}\varphi} & \mathrm{e}^{2\mathrm{j}\varphi} & 0 \\ 0 & \mathrm{e}^{2\mathrm{j}\varphi} & \mathrm{e}^{2\mathrm{j}\varphi} & 0 \\ \mathrm{e}^{-2\mathrm{j}\varphi} & 0 & 0 & \mathrm{e}^{-2\mathrm{j}\varphi} \end{pmatrix} + \frac{r_x + r_y}{2} \begin{pmatrix} 0 & 1 & 1 & 0 \\ 1 & 0 & 0 & 1 \\ 1 & 0 & 0 & 1 \\ 0 & 1 & 1 & 0 \end{pmatrix} + \begin{pmatrix} 0 & 0 & 1 & 0 \\ 0 & 0 & 0 & 1 \\ 1 & 0 & 0 & 0 \\ 0 & 1 & 0 & 0 \end{pmatrix} \tag{2.7}$$

The ideal scattering matrix for a symmetric left hand circular polarization selective

structure (LHCPSS) is

$$S^{\mathrm{CP}} = \begin{pmatrix} S_{11}^{\mathrm{RR}} & S_{11}^{\mathrm{RL}} & S_{12}^{\mathrm{RR}} & S_{12}^{\mathrm{RL}} \\ S_{11}^{\mathrm{LR}} & S_{11}^{\mathrm{LL}} & S_{12}^{\mathrm{LR}} & S_{12}^{\mathrm{LL}} \\ S_{21}^{\mathrm{RR}} & S_{21}^{\mathrm{RL}} & S_{22}^{\mathrm{RR}} & S_{22}^{\mathrm{RL}} \\ S_{21}^{\mathrm{LR}} & S_{21}^{\mathrm{LL}} & S_{22}^{\mathrm{LR}} & S_{22}^{\mathrm{LL}} \end{pmatrix} = \begin{pmatrix} 0 & 0 & \mathrm{e}^{-\mathrm{j}\phi_{\mathrm{t}}} & 0 \\ 0 & \mathrm{e}^{-\mathrm{j}\phi_{\mathrm{r}}} & 0 & 0 \\ \mathrm{e}^{-\mathrm{j}\phi_{\mathrm{t}}} & 0 & 0 & 0 \\ 0 & 0 & 0 & \mathrm{e}^{-\mathrm{j}\phi_{\mathrm{r}}} \end{pmatrix} \tag{2.8}$$

where ϕ_{r} is the phase of the reflection coefficient, and ϕ_{t} is the phase of the transmission coefficient. The expression (2.8) clearly cannot be achieved with a single surface, but we are now ready to motivate our concept design. For simplicity, assume that $r_y = 0$ and $r_x = r$, so that

$$S_{\mathrm{grid}}^{\mathrm{CP}} = \frac{r}{2} \begin{pmatrix} \mathrm{e}^{-2\mathrm{j}\varphi} & 1 & 1 & \mathrm{e}^{-2\mathrm{j}\varphi} \\ 1 & \mathrm{e}^{2\mathrm{j}\varphi} & \mathrm{e}^{2\mathrm{j}\varphi} & 1 \\ 1 & \mathrm{e}^{2\mathrm{j}\varphi} & \mathrm{e}^{2\mathrm{j}\varphi} & 1 \\ \mathrm{e}^{-2\mathrm{j}\varphi} & 1 & 1 & \mathrm{e}^{-2\mathrm{j}\varphi} \end{pmatrix} + \begin{pmatrix} 0 & 0 & 1 & 0 \\ 0 & 0 & 0 & 1 \\ 1 & 0 & 0 & 0 \\ 0 & 1 & 0 & 0 \end{pmatrix} \tag{2.9}$$

Now, assume we have two sheets separated a distance d with the relative rotation φ, both with the reflection coefficient $|r| \ll 1$. In the single scattering approximation, the total reflection coefficients from the left, with reference plane at the left-most sheet, can then be written

$$S_{11}^{\mathrm{RR}} = \frac{r}{2}\left(1 + \mathrm{e}^{-2\mathrm{j}kd}\mathrm{e}^{-2\mathrm{j}\varphi}\right) \tag{2.10}$$

$$S_{11}^{\mathrm{RL}} = S_{11}^{\mathrm{LR}} = \frac{r}{2}\left(1 + \mathrm{e}^{-2\mathrm{j}kd}\right) \tag{2.11}$$

$$S_{11}^{\mathrm{LL}} = \frac{r}{2}\left(1 + \mathrm{e}^{-2\mathrm{j}kd}\mathrm{e}^{2\mathrm{j}\varphi}\right) \tag{2.12}$$

where the exponential $\mathrm{e}^{-2\mathrm{j}kd}$ corresponds to the two-way delay between the sheets. A bounce diagram for the co-polarized reflection and transmission of the sheets, illuminated by a LHCP wave, is presented in Fig. 2. For a symmetric structure, these expressions also apply to the S_{22} elements. By choosing the separation and relative rotation of the sheets according to

$$kd = \varphi = \pi/4 \tag{2.13}$$

we can achieve polarization selectivity in reflection, since then S_{11}^{LL} is maximized and S_{11}^{RR} is minimized. Furthermore, it can be seen that by choosing the positions and rotations according to

$$kd = -\varphi = \pi/4 \tag{2.14}$$

we can achieve polarization selectivity in reflection for the orthogonal polarization, which corresponds to taking the mirror image of the previous CPSS. In addition, we can reduce the cross-polarization terms in reflection if more strip grid sheets are added. The theory of weak interaction can hence predict polarization selectivity in reflection and low cross polarization, but predicts no selectivity in transmission. This can be seen in (2.9), where the co-polarized transmission coefficients S_{21}^{RR} and S_{21}^{LL} are

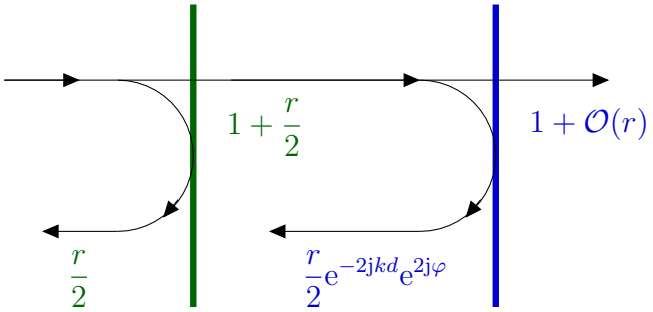

Figure 2: Bounce diagram for the co-polarized reflection and transmission from two linearly polarized layers with a relative rotation of φ, illuminated by a LHCP wave.

identical. Furthermore, reducing the cross-polarization terms by adding more layers to the structure, might result in a degradation of the insertion loss. Polarization selectivity in transmission is a higher order effect that can be anticipated by power conservation and extinction: if LHCP is being highly reflected ($|S_{11}^{\mathrm{LL}}|^2 \approx 1$), the maximum transmission is bounded by $|S_{21}^{\mathrm{LL}}|^2 \leq 1 - |S_{11}^{\mathrm{LL}}|^2 - |S_{11}^{\mathrm{RL}}|^2 - |S_{21}^{\mathrm{RL}}|^2 \ll 1$. In the same manner, if the co-polarized reflection of RHCP in (2.10) is minimized ($|S_{11}^{\mathrm{RR}}|^2 \approx 0$) it follows that $|S_{21}^{\mathrm{RR}}|^2$ is maximized, given that the cross-polarized reflection and transmission are both small ($|S_{11}^{\mathrm{LR}}|^2 + |S_{21}^{\mathrm{LR}}|^2 \approx 0$).

The main parameters defining the performance of a LHCPSS, defined in [4], are presented in (2.15),(2.16),(2.17),(2.18): the transmission and reflection parameters, insertion loss (IL) and return loss (RL), defined as the ratio of the incident power and the transmitted power in co-polarization (RHCP), and the ratio of the incident power and the reflected power in co-polarization (LHCP), and the axial ratio (AR) of the transmitted and reflected signals, which is a measure of the polarization purity of a circularly polarized wave

$$\mathrm{IL} = -20\log_{10}(|S_{21}^{\mathrm{RR}}|) \tag{2.15}$$

$$\mathrm{RL} = -20\log_{10}(|S_{11}^{\mathrm{LL}}|) \tag{2.16}$$

$$\mathrm{AR_t} = 20\log_{10}\left(\left|\frac{|S_{21}^{\mathrm{LR}}| + |S_{21}^{\mathrm{RR}}|}{|S_{21}^{\mathrm{LR}}| - |S_{21}^{\mathrm{RR}}|}\right|\right) \tag{2.17}$$

$$\mathrm{AR_r} = 20\log_{10}\left(\left|\frac{|S_{11}^{\mathrm{RL}}| + |S_{11}^{\mathrm{LL}}|}{|S_{11}^{\mathrm{RL}}| - |S_{11}^{\mathrm{LL}}|}\right|\right) \tag{2.18}$$

After investigating the circular polarization selective properties of multiple layers of strip grids, a five layer setup seems to yield a good trade-off in the transmission and reflection performance of the structure. The layout of the concept design is presented in Fig. 3, where grids of thin strips are modeled in free space, and the simulated transmission and reflection of the structure is presented in Fig. 4, where the strip width is 0.1 mm, the strip separation is 5 mm, the relative rotation is 45° and the separation between the layers is 2.5 mm (corresponding to $\lambda_0/8$ at the center frequency of operation $f = 15$ GHz).

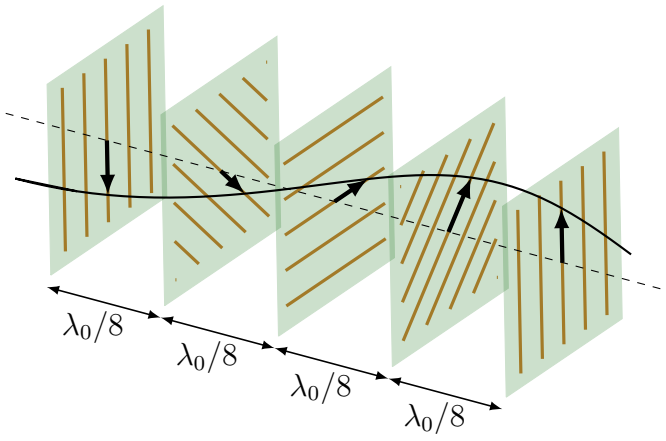

Figure 3: Concept design of a multilayer strip grid CPSS. The layers are cascaded with a separation of $\lambda_0/8$ and each layer is rotated 45° relative to the previous layer. The black line correspond to the polarization direction of a LHCP wave at a fixed time.

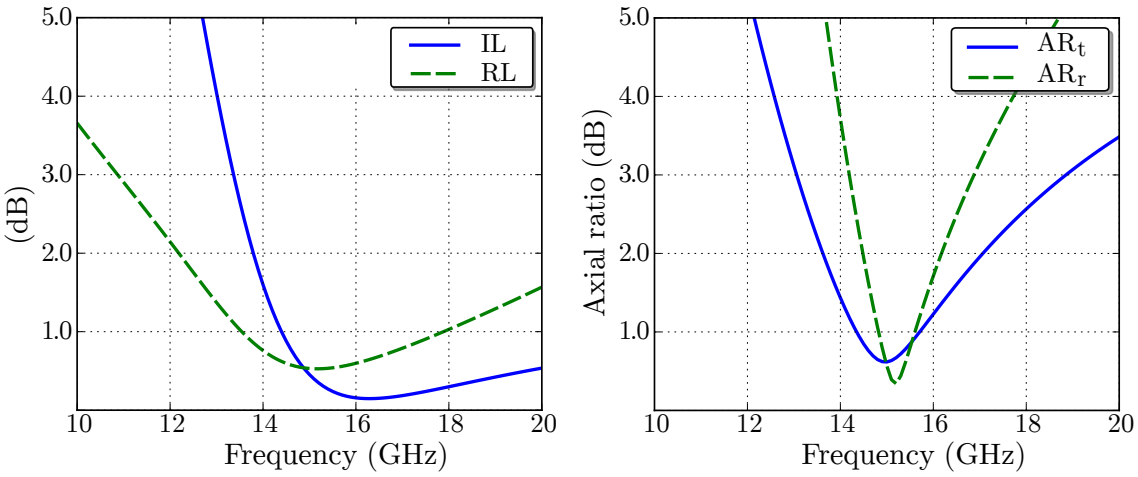

Figure 4: Simulation results for a five layer strip grid CPSS. The RHCP insertion loss and the LHCP return loss are presented in the left graph, and the RHCP axial ratio in transmission and the LHCP axial ratio in reflection are presented in the right graph. The layers are separated a distance of $\lambda_0/8$ and rotated 45° with respect to the previous layer.

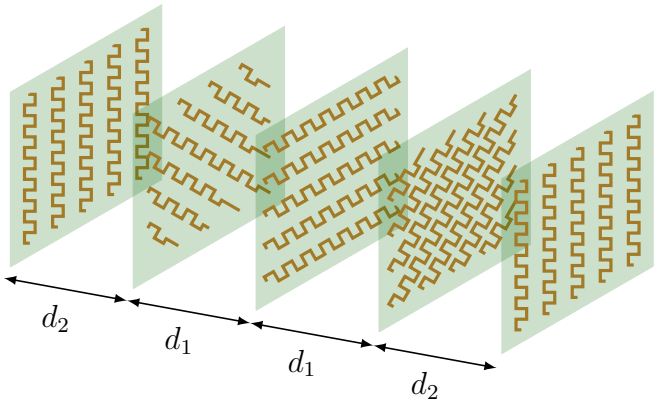

Figure 5: Concept design of a multilayer meander line CPSS. The layers are cascaded symmetrically with the separations d_1, d_2 and each layer is rotated 45° relative to the previous layer.

More design freedom is obtained by considering meandered strips, as in Fig. 5, where each strip is bent in a meandering line and the amplitude of the meandering can be used to obtain effective L and C in a broader range than what is possible with straight strips. Also, by introducing individual design parameters of each layer, and of the separation between the meander line sheets, the bandwidth of the CPSS can be greatly improved.

3 CPSS Design and Applications

When designing for space applications, the considered device needs to be able to withstand a harsh environment, involving vacuum, thermal cycling, and radiation [1, Ch. 4]. Furthermore, to reach the strict design requirements associated with satellite communication applications, it is imperative to use materials with low thermal expansion coefficients and low electromagnetic loss, typically a loss tangent around 0.001 is desirable. A realistic design of the multilayer meander line CPSS is realized by printing metal wires on thin teflon substrates through a standard etching process. The substrates are separated by low permittivity spacers, consisting of Rohacell HF31, and the substrates and spacers are bonded together using an adhesive spray 3M Scotch-Weld 76. The main characteristics of the adhesive spray are that it is suitable for the materials to be joined, and that it has a long curing time [1], thus making it possible to readjust the alignment of the materials before they are completely fixed. The material parameters of the mentioned materials are presented in Table 2. Information on the electromagnetic properties and the thickness of the adhesive layers were not available in the design phase of this work.

A unit cell was introduced to simulate the electromagnetic response of a planar test panel of infinite extent in commercial softwares. The design parameters of the CPSS can be seen in Fig. 6 and its values are given in Table 3, where P is the side length of the unit cell, the thickness of the innermost spacers is d_1, whereas the

Table 2: Material parameters of the meander line CPSS.

Material	Permittivity	Loss tangent	Thickness
Rohacell HF31, spacers	1.043	0.0017	d_1 and d_2
Arlon DiClad 880, substrates	2.170	0.0009	0.127 mm
Copper, conducting lines	$\sigma = 58$ MS/m		18 μm

Table 3: Geometrical parameters of the meander line CPSS.

Parameter	P	d_1	d_2	h_0	h_1	h_2
Value (mm)	5.20	2.61	3.81	2.44	0	2.83
Parameter	w_{0x}	w_{0y}	w_1	w_{2x}	w_{2y}	–
Value (mm)	0.46	0.58	0.21	0.25	0.17	–

outer spacers have thickness d_2. The rest of the parameters describe the meander lines, where index 0 denotes the center layer, index 1 the intermediate layers (diagonal lines), and index 2 the outermost layers. The parameters w_{ij} correspond to the width of the meander line segments of layer i, in the direction j. The height h_1 is zero since there is no meandering in the diagonal lines, which is a result of multiple optimization iterations of the structure. The total thickness of the structure is approximately 13.5 mm, which at the center frequency of operation 15 GHz corresponds to $0.68\lambda_0$. An exploded view of the unit cell geometry is presented in Fig. 7, and the optimization scheme that was used to generate the final design, and the numerical implementation of the simulation model, are described in more detail in Sections 4-5.

Two possible satellite communication applications of a CPSS are identified in [29], where a CPSS could be implemented either as curved surfaces in a CP version of the DGR presented in [5], or as a flat CP diplexer. The angles of operation of the CPSS depend on the application, and on parameters of the full reflector antenna system such as the ratio of the focal length and the diameter of the reflector (commonly referred to as f/D ratio). Typically, both the DGR and the diplexer applications require the CPSS to be able to operate at oblique angles of incidence up to $20° - 40°$ depending on the application. However, relaxed requirements can be considered at high angles of incidence due to the tapering at the edge of the beam illuminating the CPSS. In this type of applications, it is also crucial to consider the orientation of the CPSS with respect to the antennas illuminating the structure, so that the CPSS is illuminated in its preferred plane of oblique incidence.

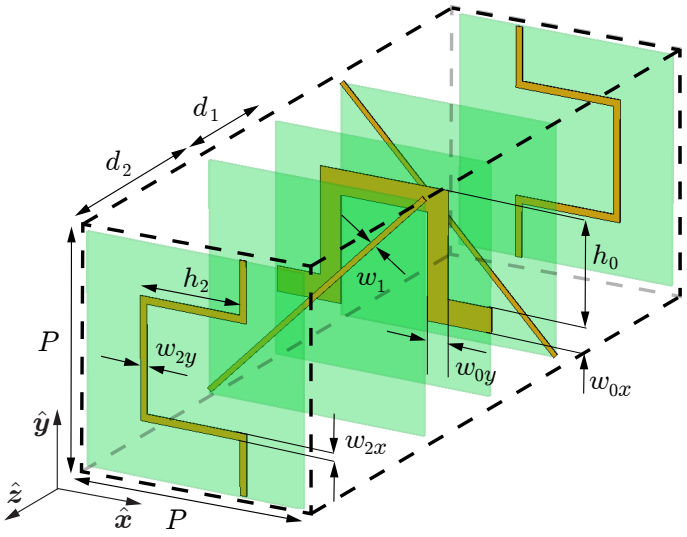

Figure 6: A unit cell of the meander line CPSS design, where the design parameters used in the design optimization process are marked out. The design is symmetric if excluding the center layer which implies that the design parameters of the back layers are the same as those of the first two layers.

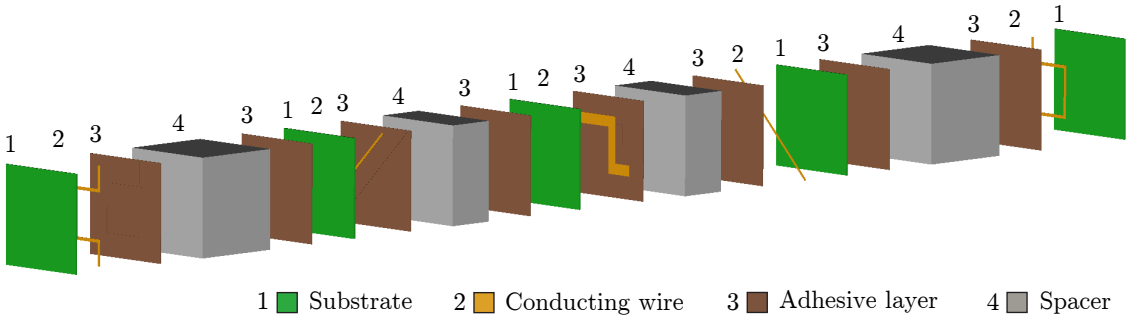

Figure 7: Exploded view of the meander line CPSS implemented for optimization in a commercial software, with realistic, lossy, materials suitable for space applications. The metal wires are printed on substrates that are separated by low permittivity spacers, and the substrates and spacers are bonded together using thin adhesive films.

4 Optimization Scheme

The CPSS design was optimized using a three-step process, as can be seen in Fig. 8. First, an analytical model implemented in Python was used to find the parameter region of interest for further local optimization (see www.python.org and www.scipy.org). The code uses transmission line theory to model the low permittivity foam and the substrates as propagation matrices, and each interface between the different materials is modeled as a matching matrix [7]. The meander line sheets are modeled as lumped reactances by using explicit formulas for the effective capacitance and inductance of meander lines in [14], which were implemented in [6]. The whole structure is thus described by a cascaded system of T-matrices, which can easily be transformed to yield the total scattering matrix S of the CPSS structure. This implementation only considers one mode for each polarization and does not include the effect of higher order modes from coupling between subsequent layers of the CPSS. Depending on the geometry of the structure under study, this might cause a discrepancy between the analytic model and full wave results. The parameters were optimized using the SciPy optimization package routine `fmin`, which is a downhill simplex algorithm, by minimizing a penalty function of the form

$$F = \frac{1}{f_2 - f_1} \int_{f_1}^{f_2} (a_1 \mathrm{AR_r} + a_2 \mathrm{AR_t} + a_3 \mathrm{RL} + a_4 \mathrm{IL}) \, \mathrm{d}f \tag{4.1}$$

where f is the frequency and a_i are weights assigned in the optimization process. $\mathrm{AR_r}$ and RL are the axial ratio and return loss of the reflected signal for incident LHCP, $\mathrm{AR_t}$ and IL are the axial ratio and insertion loss of the transmitted signal for incident RHCP, and all these quantities are defined in decibels. A few thousand design candidates were generated in a few minutes, and a more detailed discussion of the analytical model is presented in [32].

The found parameter values were then imported from the python model into a full wave simulation software, Computer Simulation Technology Microwave Studio (CST MWS), where further optimization was performed at a reasonable accuracy and speed. The trust region framework optimizer was used to find the best design in a local parameter space, where the parameters were typically varied $\pm 20\%$ with respect to the initial design. A tetrahedral mesh was utilized consisting of about 35 000 elements, using 2.4 GB of RAM on a dual core Intel Core i7, 3.5 GHz workstation, and finishing one design simulation in 17 minutes. About a hundred designs were generated in one full optimization iteration of 28 hours. In some design cases, a few iterations of this full wave optimization were necessary to reach the goals, using different weights a_i and frequency bands in the penalty function F. Finally, the resulting design was verified using a finer simulation mesh, leading to longer simulation times.

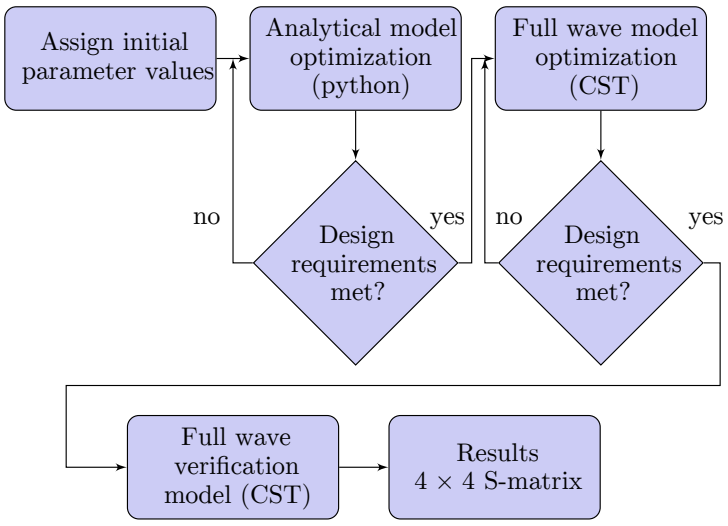

Figure 8: Optimization scheme, utilizing an analytical model implemented in Python and full wave simulation models in CST MWS.

5 Simulation Results

The meander line CPSS design was simulated in CST MWS, as a unit cell model, in the full wave frequency domain finite element solver that utilizes Floquet mode analysis. At the design stage, the electromagnetic properties and the thickness of the adhesive layers were unknown to the authors, but these layers were expected to be very thin, and thus the adhesive layers were excluded from the simulation model. In Figs. 9-10 simulation results after multiple optimization iterations using the analytic model, referred to as design 1, are presented alongside simulation results after multiple optimization iterations in CST, referred to as design 2. Good agreement between the analytic model and full wave simulations of design 1 can be seen in RL, but the IL and AR in reflection and transmission deviate. This difference is mainly due to the previously mentioned higher order mode excitations that are not considered in the analytic model.

The mesh convergence of the final design was investigated, and it was concluded that the results had converged to an accuracy of 0.02 dB with respect to IL, RL, and AR, when using a mesh consisting of 75 000 mesh elements, corresponding to 16 steps per wavelength mesh setting. A simulation with the described settings was using 10 GB of RAM and finishing one simulation in about one hour. When comparing the simulation results using the finer mesh setting to the results generated in the optimization scheme, which used 35 000 mesh elements, corresponding to 12 steps per wavelength mesh setting, a deviation smaller than 0.07 dB is observed, see Figs. 9-10. In [32], the mesh convergence of the CPSS was studied in detail using finer mesh settings and comparing two separate simulation softwares.

Simulation results of the final design were generated for multiple incidence angles using the fine mesh and are presented in Figs. 11–12. The results indicate that

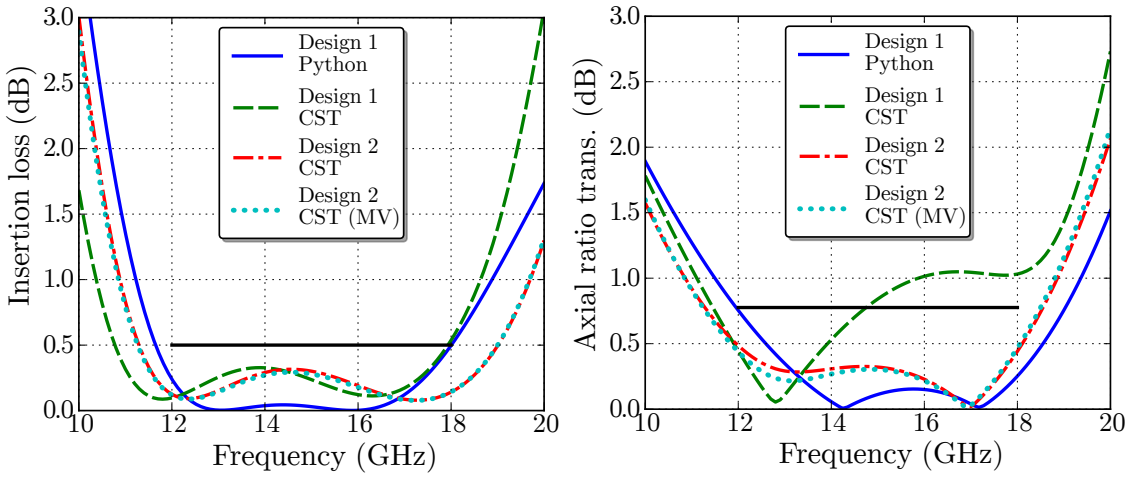

Figure 9: Simulation results of the multilayer CPSS at normal incidence. The solid and dashed curves correspond to simulation results from the analytic model and from CST after optimization in the analytic model. The dash-dotted and the dotted curves correspond to simulation results from CST after full wave optimization using a normal mesh and a finer mesh for verification, respectively. In the left plot is the RHCP IL, and in the right plot is the AR of the corresponding transmitted signal. The solid black lines are the design requirements defined in [4].

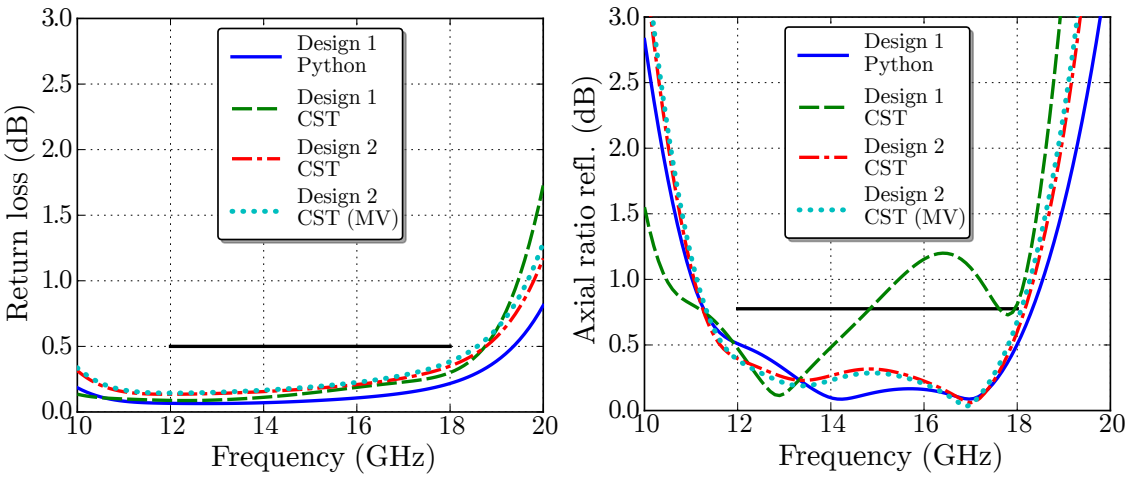

Figure 10: Simulation results of the multilayer CPSS at normal incidence. The solid and dashed curves correspond to simulation results from the analytic model and from CST after optimization in the analytic model. The dash-dotted and the dotted curves correspond to simulation results from CST after full wave optimization using a normal mesh and a finer mesh for verification, respectively. In the left plot is the LHCP RL, and in the right plot is the AR of the corresponding reflected signal. The solid black lines are the design requirements defined in [4].

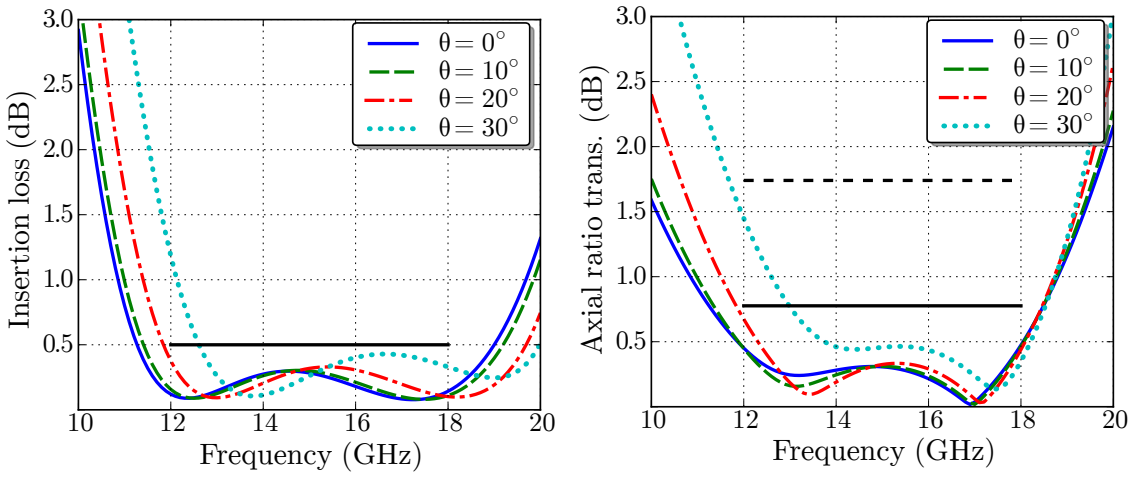

Figure 11: Simulation results of the multilayer CPSS at different angles of incidence, in the plane $\varphi = 225°$. In the left plot is the RHCP IL, and in the right plot is the AR of the corresponding transmitted signal. The solid black lines are the design requirements defined in [4], and the dashed black lines are relaxed requirements of AR $< 1.74\,\mathrm{dB}$.

the fractional bandwidth of the design is approximately 45%, which is a significant increase compared to what has previously been presented [2, 3, 10, 12, 17, 18, 19, 20, 21, 23, 24, 27, 28, 33, 34, 35] as can be seen in the bandwidth comparison in Table 1. Furthermore, the results indicate a significant stability with respect to variations in the angle of incidence, especially in the range $\theta \in (0°, 20°)$. The performance of the CPSS has been compared to the requirements put forward in [4] and used in [29] for a $\mathrm{K_u}$-band scenario:

- Insertion loss and return loss better than 0.5 dB.
- Axial ratio better than 0.78 dB.

The axial ratio requirement corresponds to 27 dB cross polarization discrimination, which can be relaxed to 20 dB (AR better than 1.74 dB) at higher angles of incidence. As can be seen in Figs. 11-12, these requirements are satisfied in the incidence plane $\varphi = 225°$, up to a 20° angle of incidence in the entire $\mathrm{K_u}$ band, or 30° angle of incidence for the relaxed AR requirements, except for a small penalty in IL at lower frequencies.

To evaluate how the performance of the structure varies with respect to the oblique angle of incidence (θ) in all possible incidence planes (φ), the scattering matrix of the structure was computed for every combination of $\theta = 0°, 5°, \ldots, 85°$ and $\varphi = 0°, 5°, \ldots, 355°$, corresponding to 1296 simulations. In Figs. 13-14 simulation results are presented at the fixed frequencies $f = 13, 15, 17\,\mathrm{GHz}$, utilizing a coarser mesh setting of 10 steps per wavelength, corresponding to about 22 000 mesh elements. To speed up these computations, the simulations were divided between multiple work stations, and multiple simulations were run in parallel on each

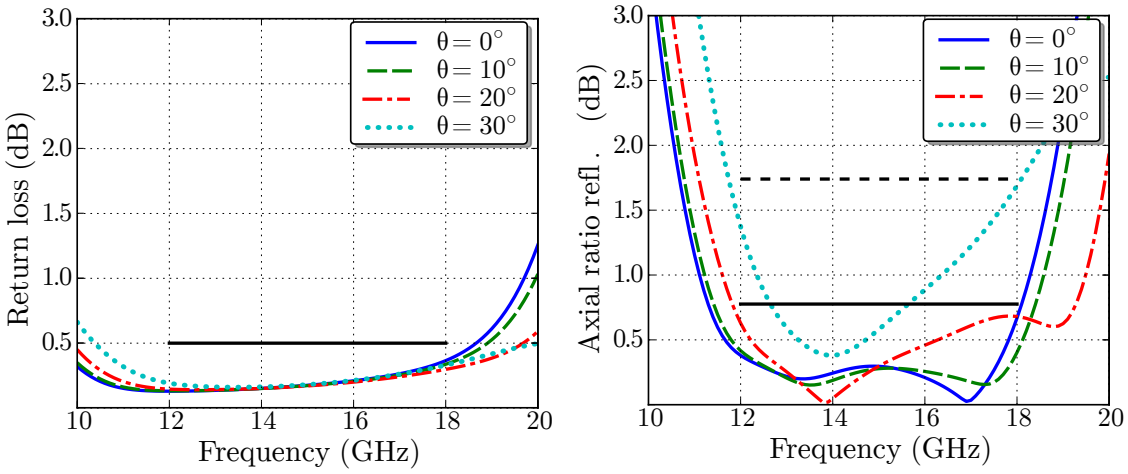

Figure 12: Simulation results of the multilayer CPSS at different angles of incidence, in the plane $\varphi = 225°$. In the left plot is the LHCP RL, and in the right plot is the AR of the corresponding reflected signal. The solid black lines are the design requirements defined in [4], and the dashed black lines are relaxed requirements of AR $< 1.74\,\mathrm{dB}$.

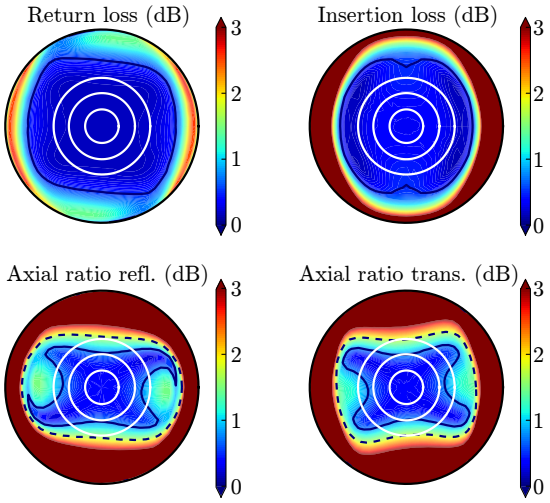

Figure 13: Simulation results for front side illumination of the CPSS at the center frequency of operation $f_0 = 15$. The left plots show the return loss and axial ratio of the reflected LHCP signal, the right plots correspond to the insertion loss and the axial ratio of the transmitted RHCP signal, and all values are in dB. The white circles indicate $\theta = 10°, 20°, 30°$, the solid black contours are the design requirements defined in [4], and the dashed black contours are relaxed requirements of AR $<$ 1.74 dB.

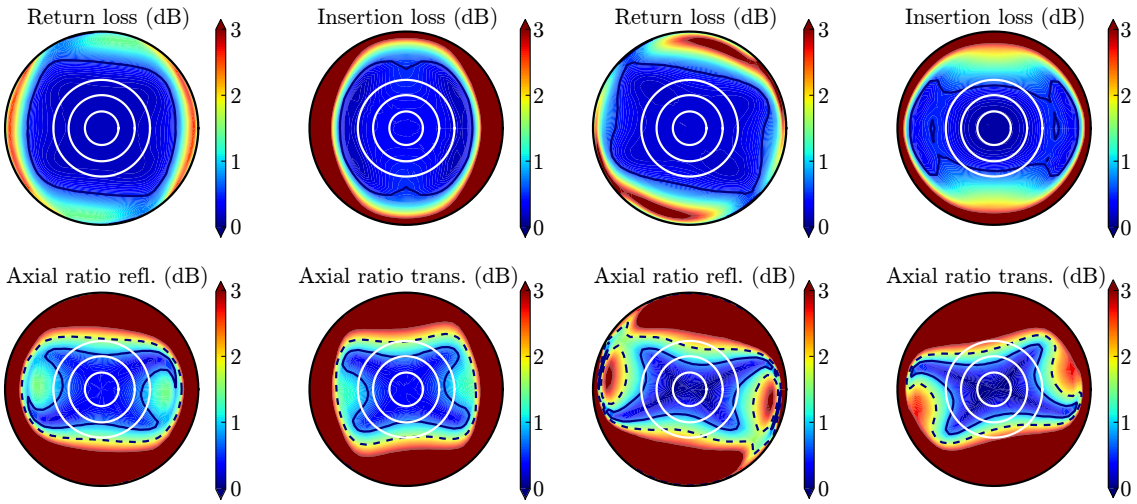

Figure 14: Simulation results for front side illumination of the CPSS at the frequency $f = 13\,\mathrm{GHz}$ to the left, and at the frequency $f = 17\,\mathrm{GHz}$ to the right.

computer. The full parameter sweep was completed in about 367 hours of CPU time.

Simulating the scattering from the structure in CST MWS at each angle of incidence of interest resulted in scattering data at a great number of frequency points over the full frequency band of interest. This follows from the fact that the program utilizes automatic frequency sampling in a few points and then applies curve fitting to the results in between the sample points. The radius in Figs. 13–14 corresponds to $\sin\theta$ so that the Cartesian coordinates are $x = \sin\theta\cos\varphi$, and $y = \sin\theta\sin\varphi$, with the z-axis pointing towards the reader. It is seen that the performance of the CPSS at oblique angles of incidence is maximized in incidence planes close to $\varphi = 45°, 135°$. The reason why the structure has two preferred incidence planes is due to the rotational symmetry of the design. Furthermore, the symmetry of the structure implies that the scattering performance is symmetric with respect to the sign of the incidence angle θ, meaning maximum performance also for $\varphi = 225°, 315°$. When comparing the results in Figs. 13-14 it can be seen that the stability of the performance of the structure varies with the frequency of the incident signal, and that the performance at more oblique angles of incidence deteriorate for frequencies at the outer parts of the design band of operation. A small discrepancy can be observed between the results in Figs. 11-12 and in Figs. 13-14. This is caused by the fact that a coarser mesh was used when generating the results in Figs. 13-14.

The same type of performance evaluation as in Figs. 13-14 is found in [9], where the designs by Pierrot [24], Morin [23], and Tilston [35] were studied. There it is shown that all three designs have one preferred incidence plane of operation (identifying directions $\pm\theta$ as being in the same plane). The fact that the novel CPSS presented in this paper possesses multiple incidence planes of operation, results in a significant design freedom for implementations in satellite communication systems.

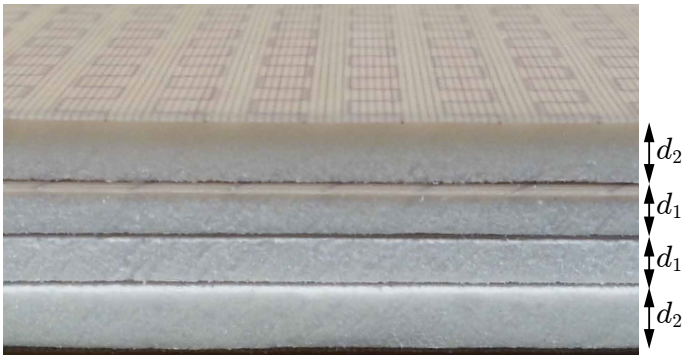

Figure 15: Side view of the manufactured test panel of total size 58x58x1.4 cm

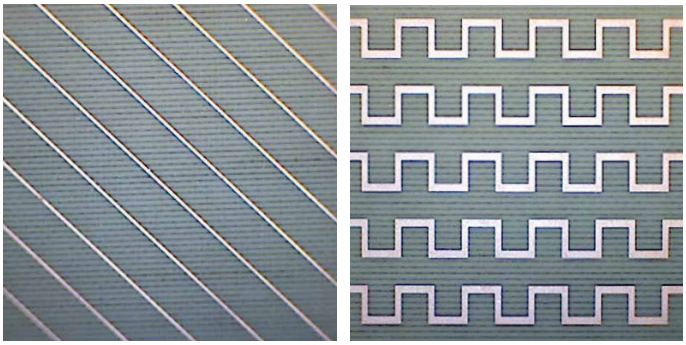

Figure 16: Printed teflon substrates, consisting of Arlon DiClad 880, with a relative permittivity of 2.17, and a thickness of 0.127 mm. The period of the printed pattern is the same in all five layers, where $P = 5.38$ mm.

6 Manufactured Test Panel and Measurements

A prototype of the optimized CPSS design was manufactured as can be seen in Fig. 15. The width and height of the test panel is 58 cm, and the total thickness of the structure is 13.7 mm, which should be compared to the total thickness of the simulated structure of 13.5 mm. The thickness of the spacers were controlled to a tolerance of ± 0.2 mm in the manufacturing process, and the effect of the adhesive layers on the total thickness of the structure is unknown. The fact that the thickness of the manufactured test panel only deviates from the desired value by 0.2 mm is a desirable outcome. The full test panel was assembled by joining the thin teflon sheets, see Fig. 16, to the Rohacell spacers by applying a thin layer of adhesive spray, and then applying an even pressure over the full surface for an extended amount of time. Since the full prototype consists of five layers of substrates, and four layers of spacers, a total of eight adhesive layers were applied to the structure one layer at a time using the above mentioned technique. When the full prototype was assembled, protective tape was added to the edges to avoid cracks in the spacers and failure in the bonding.

Transmission and reflection measurements of the manufactured prototype were carried out at Lund University, and the measurement setup in transmission is seen

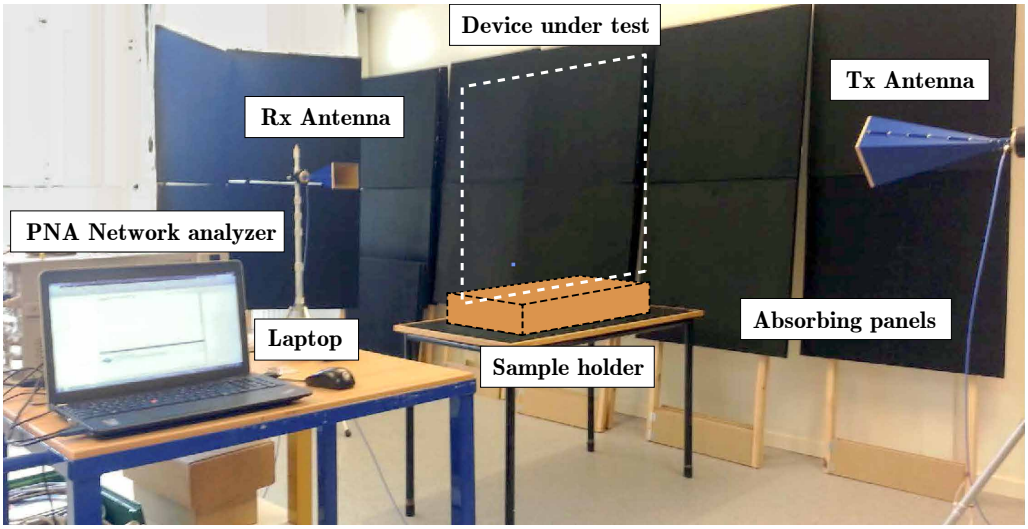

Figure 17: Measurement setup at Lund University, Sweden. The manufactured CPSS test panel was measured using single feed, linearly polarized, standard gain horn antennas in the frequency range $10\,\mathrm{GHz} < f < 20\,\mathrm{GHz}$.

in Fig. 17. The test panel was illuminated using two rectangular standard gain horn antennas, SATIMO SGH 1240, each with a cross polarization discrimination of about 40 dB. Two free standing antenna fixtures were separated a distance of approximately 3 m, at a height of 1.4 m, and a table with the device under test (DUT) was placed at the center of the setup. The antennas were connected to a vector network analyzer, Agilent E8364b, which in turn was controlled by a laptop through a GPIB connection and a Matlab script. In the reflection case, both antennas were placed at the same side of the DUT, at a small oblique angle $\theta \approx 3^\circ$ due to the size of the antenna apertures.

To reduce the amount of multipath components in the measurement data, portable absorbing panels as can be seen in Fig. 17 were placed around the setup during the measurements. That way, the user and the electronics controlling the measurement were shielded from the radiating antennas. Since linearly polarized antennas were used in the measurements, the circular polarization response of the test panel was synthesized from four linearly polarized components. To achieve a similar signal to noise ratio (SNR) in all four linearly polarized components measured, the transmitting and receiving antennas were oriented 45 degrees with respect to each other in each measurement. The advantage of this technique is that when each scattering matrix component of the DUT is normalized with a corresponding reference measurement, all reference measurements have similar and high SNR. This implied that, instead of synthesizing circular polarization through the traditionally used 90 degrees antenna orientations: XX, YY, XY, YX the four 45 degrees components XU, XV, YU, YV were measured, see Fig. 18.

The four scattering matrix transmission components $S_{21}^{\mathrm{XU}}, S_{21}^{\mathrm{YU}}, S_{21}^{\mathrm{XV}}, S_{21}^{\mathrm{YV}}$ were measured for the test panel and for a free space through reference setup. These four components of the DUT were each normalized with its reference components and

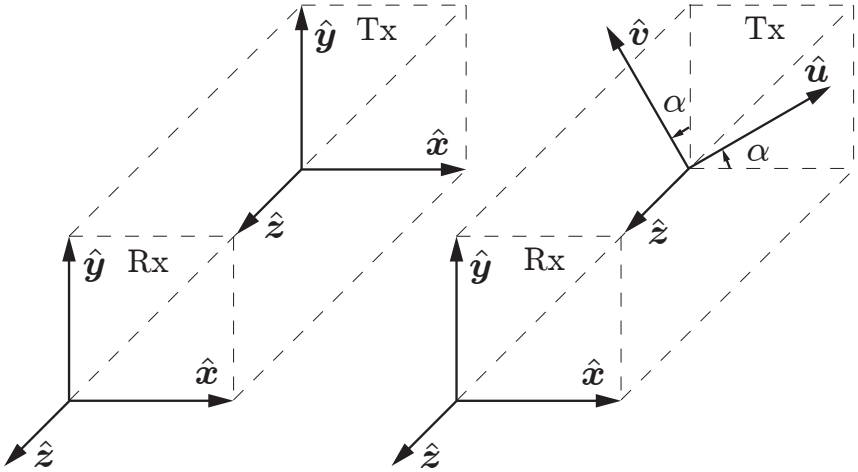

Figure 18: A principal sketch of the antenna orientations for synthesizing circular polarization from linear polarization measurements. To the left, the main directions of the transmitting and receiving antennas are aligned, and the relative rotation between the antennas is either 0° or 90°. To the right, the main directions of the transmitting and receiving antennas are not aligned, and if the antenna orientation angle $\alpha = 45°$, the relative rotation between the antennas is always 45°.

then transformed to the traditional linear co- and cross polarization components $S_{21}^{\mathrm{XX}}, S_{21}^{\mathrm{YX}}, S_{21}^{\mathrm{YY}}, S_{21}^{\mathrm{XY}}$ through the matrix rotation relation

$$S_{21}^{\mathrm{LP}} = \begin{pmatrix} S_{21}^{\mathrm{XX}} & S_{21}^{\mathrm{XY}} \\ S_{21}^{\mathrm{YX}} & S_{21}^{\mathrm{YY}} \end{pmatrix} = \begin{pmatrix} S_{21}^{\mathrm{XU}} & S_{21}^{\mathrm{XV}} \\ S_{21}^{\mathrm{YU}} & S_{21}^{\mathrm{YV}} \end{pmatrix} \begin{pmatrix} \cos 45° & \sin 45° \\ -\sin 45° & \cos 45° \end{pmatrix} \tag{6.1}$$

In the same manner, the four scattering matrix reflection components S_{11}^{XU},S_{11}^{YU}, S_{11}^{XV},S_{11}^{YV} were measured for the test panel and for a reference reflection setup, by adding aluminum foil to the front surface of the test panel. These four components were then normalized and transformed to the traditional linear co- and cross polarization components $S_{11}^{\mathrm{XX}}, S_{11}^{\mathrm{YX}}, S_{11}^{\mathrm{YY}}, S_{11}^{\mathrm{XY}}$ using the same matrix rotation relation as in (6.1). The circular polarization response was then determined applying the relation (2.6) to the linear polarization scattering matrix.

To remove the remaining multipath components from the measured data, time gating was implemented by applying a Gaussian window function to the data in the time domain. The relative measurement error of the setup when rotating the antennas, mainly caused by misalignment of the antennas, was measured in transmission and reflection to approximately ±0.3 dB in amplitude, and ±3° in phase. Part of the effect of antenna misalignments are mitigated by the normalization of each component with a reference measurement, which implies that these values can be seen as a worst case scenario. The AR of a free space measurement in transmission was better than 0.5 dB, and in reflection the AR of a conducting reference panel was better than 0.7 dB, over the full frequency range of interest $10\,\mathrm{GHz} < f < 20\,\mathrm{GHz}$. These results indicate that measured AR values below 0.5 dB in transmission and below 0.7 dB in reflection have to be considered uncertain.

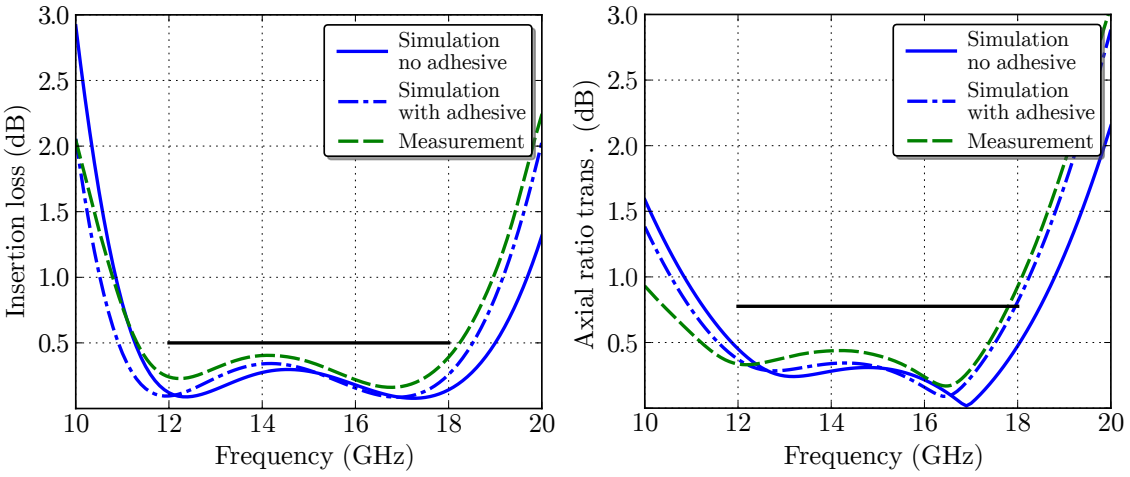

Figure 19: Transmission measurement results of the manufactured test panel, at normal incidence ($\theta = 0°, \varphi = 0°$). The left plot shows the RHCP insertion loss from simulated and measured data, and the right plot shows the RHCP AR. The solid black lines are the design requirements defined in [4].

Table 4: Bandwidth over which the CPSS satisfies all requirements IL and RL better than 0.5 dB, and AR_t and AR_r better than 0.78 dB. K_u coverage relates to the target band 12 GHz $< f <$ 18 GHz.

	Min. freq.	Max. freq.	Total BW	K_u coverage
Simulated	11.4 GHz	18.2 GHz	45.9%	100%
Measured	11.3 GHz	17.2 GHz	42.0%	86.7%

The measurement results presented in Figs. 19-20 show a clear selectivity with respect to circular polarizations, both in transmission and reflection. The bandwidths of the simulated and measured CPSS with respect to satisfying all the requirements in IL, RL, AR_t, and AR_r, are summarized in Table 4. The total bandwidth exceeds 40% in both simulations and measurements. A slight shift down in frequency is observed when comparing the measured data to the simulated results, reducing the coverage of the targeted K_u band to 86.7%. The shift in frequency might be caused by the impact of the adhesive spray on the thickness of the structure, the effective conductivity of the spacers, as well as the manufacturing uncertainty of the spacers of ± 0.2 mm. Also, a slight increase in level can be noticed in the measured curves in Figs. 19-20, which might be caused by air bubbles in the adhesive layers, and additional material losses not accounted for in the simulations. Also, misalignment between the subsequent substrates is a source of error that can affect the AR of the test panel.

In order to account for the impact of the adhesive spray on the performance of the test panel, a simulation model was implemented with adhesive layers added to the structure. Since the thickness of the manufactured test panel was observed to be

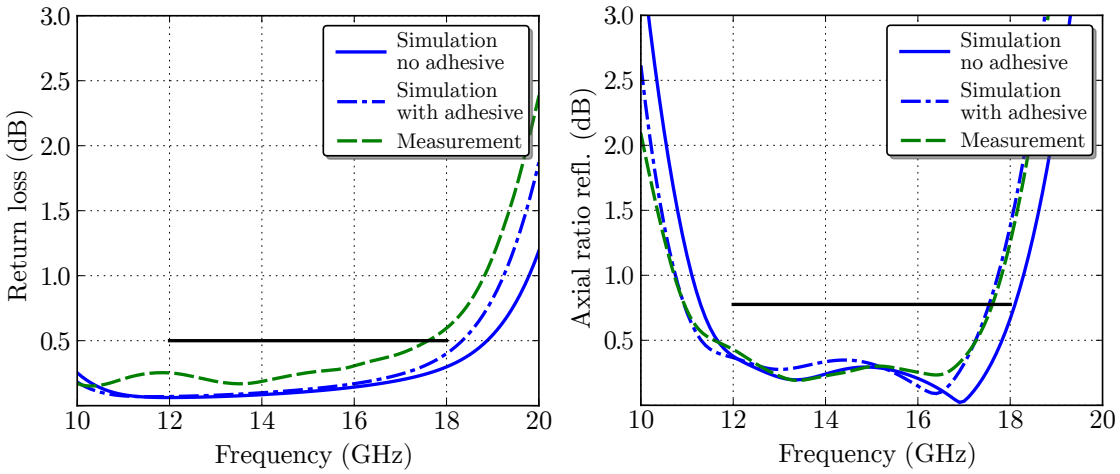

Figure 20: Reflection measurement results of the manufactured test panel, at normal incidence ($\theta = 3°, \varphi = 0°$). The left plot shows the LHCP return loss from simulated and measured data, and the lower right shows the LHCP AR. The solid black lines are the design requirements defined in [4].

0.2 mm thicker than the simulated structure, this difference was distributed evenly over the eight adhesive layers. The material parameters of the adhesive were chosen according to comparable adhesive films commonly used for similar applications, for instance the LTM123 used in [8], having $\epsilon_r = 2.77$ and $\tan\delta = 0.005$. The thickness of the adhesive layers was calculated from the deviation in thickness between the simulation model and the manufactured design, resulting in $t = 0.2/8 = 0.025$ mm.

The simulated performance of the structure, with adhesive layers, is compared to measurements in Figs. 19-20, and the results indicate that adding adhesive layers to the simulations improve the agreement between the simulated and measured data both in transmission and reflection. However, the IL curves in Fig. 19 and the RL curves in Fig. 20 still show a small discrepancy. The difference in RL can possibly be caused by a misalignment in the measurement setup, as this was found to be especially sensitive in reflection. A small discrepancy can also still be noticed in the AR curves between simulations and measurements. As previously mentioned, this is most likely caused by measurement errors, misalignment between the meander line substrates, as well as the uncertainty of the Rohacell spacer thickness.

7 Conclusions

This paper presents a novel circular polarization selective structure based on multi-layer meander line sheets. Compared to previous CPSS designs, the structure shows significant improvements in bandwidth and stability with respect to variations in the angle of incidence. The performance of the structure was evaluated both as a function of frequency, as well as over all possible angles of incidence at the edges and center of the frequency band, and it is shown to possess two preferred incidence planes of operation. A concept prototype was manufactured and the measurement

results are in good agreement with simulation data. The high performance of this design makes it a good candidate for implementations in future satellite communication systems, either as a flat circular polarization diplexer or as a curved shared aperture reflector.

Acknowledgments

The authors of this paper kindly acknowledge Ron van Hoorn and Oliver Krause at Evonik for providing Rohacell samples for the manufacturing of the test panel, Lars Hedenstjerna at Lund University for manufacturing the fixtures for the measurement setup, Christian Nelson at Lund University for assisting in the assembly of the test panel, and Peter Balling, Antenna Systems Consulting ApS (ASC), for the implementation of the analytical free space meander line models. The work reported in this paper was performed under ESA Contract No. 4000108854/13/NL/MH.

References

[1] *3M 76 Scotch Weld Spray Long Open Time Adhesive*. 2016-07-09.

[2] S. M.A.M. H. Abadi and N. Behdad. "A broadband, circular-polarization selective surface". *Journal of Applied Physics* 119 (24) (2016): p. 244901.

[3] S. M.A.M. H. Abadi and N. Behdad. "Wideband linear-to-circular polarization converters based on miniaturized-element frequency selective surfaces". *IEEE Trans. Antennas Propag.* 64 (2) (2016): pp. 525–534.

[4] M. Albani, P. Balling, L. Datashvili, G Gerini, P. Ingvarson, K. Pontoppidan, M. Sabbadini, D. Sjöberg, S. Skokic, and G. Vecchi. "Concepts for polarising sheets & "dual-gridded" reflectors for circular polarisation". In: *ICECom Proceedings*. 2010, pp. 1–4.

[5] M. Baunge, H. Ekström, P. Ingvarson, and M. Petersson. "A new concept for dual gridded reflectors". In: *Proceedings of the fourth European Conference on Antennas and Propagation (EuCAP)*. IEEE. 2010, pp. 1–5.

[6] R. S. Chu and K. M. Lee. "Radiation impedance of a dipole printed on periodic dielectric slabs protruding over a ground plane in an infinite phased-array". *IEEE Trans. Antennas Propag.* 35 (1) (1987): pp. 13–25.

[7] R. E. Collin. "Foundations for Microwave Engineering". Second. McGraw-Hill, 1992.

[8] J. A. Encinar, L. S. Datashvili, J. A. Zornoza, M. Arrebola, M. Sierra-Castañer, J. L. Besada-Sanmartin, H. Baier, and H. Legay. "Dual-polarization dual-coverage reflectarray for space applications". *IEEE Trans. Antennas Propag.* 54 (10) (2006): pp. 2827–2837.

[9] A Ericsson and D Sjöberg. "A performance study of circular polarization selective structures". In: *Proceedings of the 9th European Conference on Antennas and Propagation (EuCAP)*. IEEE, 2015.

[10] A. Ericsson and D. Sjöberg. "A resonant circular polarization selective structure of closely spaced wire helices". *Radio Science* 50 (8) (2015): pp. 804–812.

[11] A. Ericsson and D. Sjöberg. "Design and analysis of a multilayer meander line circular polarization selective structure". *IEEE Trans. Antennas Propag.* 65 (8) (2017): pp. 4089–4101.

[12] V. Fusco and B Nair. "Circular polarisation selective surface characterisation and advanced applications". *IEE Proceedings Microwaves Antennas and Propagation* 153 (3) (2006): p. 247.

[13] J. K. Gansel, M. Thiel, M. S. Rill, M. Decker, K. Bade, V. Saile, G. von Freymann, S. Linden, and M. Wegener. "Gold helix photonic metamaterial as broadband circular polarizer". *Science* 325 (5947) (2009): pp. 1513–1515.

[14] L Goldstone. "A compact broadband CP MM wave horn". In: *Antennas and Propagation Society International Symposium, 1982.* Vol. 20. IEEE. 1982, pp. 640–643.

[15] *IEEE Standard Test Procedures for Antennas*. IEEE, 1979.

[16] W. A. Imbriale, S. S. Gao, and L. Boccia, eds. "Space Antenna Handbook". Wiley, 2012.

[17] M Joyal and J Laurin. "Analysis and design of thin circular polarizers based on meander lines". *IEEE Trans. Antennas Propag.* 60 (6) (2012): pp. 3007–3011.

[18] M Joyal and J Laurin. "Design and analysis of a cascade circular-polarization-selective surface at K band". *Antennas and Propagation, IEEE Transactions on* 62 (6) (2014): pp. 3043–3052.

[19] M.-A. Joyal and J.-J. Laurin. "A cascaded circular-polarization-selective surface at K band". In: *Antennas and Propagation (APSURSI), 2011 IEEE International Symposium on.* IEEE. 2011, pp. 2657–2660.

[20] I. Lopez and J.-J. Laurin. "A circular polarization selective surface implemented on a flexible substrate". *IEEE Trans. Antennas Propag.* 62 (7) (2014): pp. 3847–3852.

[21] I. Lopez and J.-J. Laurin. "Alternative topologies of circular polarization selective surfaces based on modifications of the Pierrot cell". *IEEE Trans. Antennas Propag.* 63 (4) (2015): pp. 1465–1472.

[22] N. Marcuvitz. "Waveguide Handbook". McGraw-Hill, 1951.

[23] G. Morin. *Circular polarization selective surface made of resonant spirals.* 1994.

[24] R. Pierrot. *Reflector for circularly polarized waves.* 1970.

[25] S. Rao, L. Shafai, and S. K. Sharma. "Handbook of Reflector Antennas and Feed Systems Volume III: Applications of Reflectors". Artech house, 2013.

[26] J. E. Roy. "A reciprocal cpss molecule". In: *Antenna Technology and Applied Electromagnetics (ANTEM), 2016 17th International Symposium on.* IEEE. 2016, pp. 1–2.

[27] J. E. Roy and L. Shafai. "Reciprocal circular-polarization-selective surface". *Antennas and Propagation Magazine, IEEE* 38 (6) (1996): pp. 18–33.

[28] J. Sanz-Fernandez, E. Saenz, and P. de Maagt. "A circular polarization selective surface for space applications". *IEEE Trans. Antennas Propag.* 63 (6) (2015): pp. 2460–2470.

[29] J. Sanz-Fernandez, E. Saenz, P. de Maagt, and C. Mangenot. "Circular polarization selective surface for dual-optics CP offset reflector antennas in Ku-band". In: *Proceedings of the 6th European Conference on Antennas and Propagation (EuCAP)*. IEEE. 2012, pp. 2683–2687.

[30] M. Selvanayagam and G. V. Eleftheriades. "Design and measurement of tensor impedance transmitarrays for chiral polarization control". *Microwave Theory and Techniques, IEEE Transactions on* 64 (2) (2016): pp. 414–428.

[31] D. Sjöberg. "Circuit analogs for wave propagation in stratified structures". In: *Wave Propagation in Materials for Modern Applications*. Ed. by A. Petrin. InTech, 2010, pp. 489–508.

[32] D. Sjöberg and A. Ericsson. "A multi layer meander line circular polarization selective structure (MLML-CPSS)". In: *Proceedings of the 8th European Conference on Antennas and Propagation (EuCAP)*. IEEE. 2014, pp. 464–468.

[33] W. Tang, G. Goussetis, N. J. Fonseca, H. Legay, E. Saenz, and P. de Maagt. "Study of coupled split-ring resonator arrays for circular polarization selective surface". In: *Antennas and Propagation & USNC/URSI National Radio Science Meeting, 2015 IEEE International Symposium on*. IEEE. 2015, pp. 362–363.

[34] I.-Y. Tarn and S.-J. Chung. "A new advance in circular polarization selective surface-a three layered cpss without vertical conductive segments". *IEEE Trans. Antennas Propag.* 55 (2) (2007): pp. 460–467.

[35] D. Tilston, M. Tilston, S. Tilston, W. V. Tilston, and T. Tralman. *Polarization selective surface for circular polarization*. 1991.

[36] R. Torres and M. Catedra. "Analysis and design of a two-octave polarization rotator for microwave frequency". *IEEE Trans. Antennas Propag.* 41 (2) (1993): pp. 208–213.

[37] Y Zhao, M. Belkin, and A Alú. "Twisted optical metamaterials for planarized ultrathin broadband circular polarizers". *Nature Communications* 3 (2012): p. 870.